Carbon Nanostructures Derived from In Situ Grown ZIF Nanocages within Bacterial Cellulose for AC-Filtering Electrochemical Capacitors

Rishav Baranwal[1], Xueyan Lin[1], Yinxuan Qiao[2], Haiyan Tan[3], Michael Goryll[2], Zhaoyang Fan[2*]

[1]School for Engineering of Matter, Transport & Energy, Arizona State University, Tempe, AZ 85281, USA

[2]School of Electrical, Computer and Energy Engineering, Arizona State University, Tempe, AZ 85281, USA

[3]Institute of Materials Science, University of Connecticut, Storrs, CT 06269, USA

*Contact author: zyfan@asu.edu

Abstract

Electrochemical capacitors (ECs) offer superior specific capacitance for energy storage compared to traditional electrolytic capacitors but face limitations in alternating current (AC) filtering due to the need for balancing fast response and high capacitance. This study addresses these challenges by developing a freestanding nanostructured carbon electrode, derived from the rapid carbonization of bacterial cellulose (BC) embedded with zeolitic imidazolate framework 8 (ZIF-8) and in-situ formed carbon nanotubes (CNTs). The electrode exhibits an exceptionally low area resistance of 9.8 mΩ cm² and a high specific capacitance of 2.1 mF cm^{-2} at 120 Hz, maintaining performance even at high frequencies. Stacking these electrodes enhances the capacitance to 5.3 mF cm^{-2}, with the phase angle degrading to −74.4° at 120 Hz; however, they retain a phase angle below −45° up to approximately 50 kHz, demonstrating excellent high-frequency performance. Furthermore, connecting three aqueous units in series as an integrated cell or utilizing organic electrolytes extends the voltage window to 2.4 V, enhancing their suitability for high-voltage applications. Ripple voltage analysis under various loads and frequencies indicates effective filtering capabilities, highlighting the potential of these nanostructured ECs for next-generation electronic applications.

Keywords: Electrochemical capacitors; AC filtering; Bacterial Cellulose; ZIF-8; Metal organic frameworks.

Introduction:

Despite their vital role, bulky aluminum electrolytic capacitors (AECs) with low specific capacitance still dominate the filtering and decoupling capacitor market for frequencies below approximately 1 MHz. Electrochemical capacitors (ECs) offer a promising alternative with higher specific capacitances; however, they typically have a time constant (τ_{RC}) of at least 1 second at 120 Hz, which is inadequate for effective line-frequency filtering that requires a phase angle ($\varphi = -\arctan\frac{1}{\omega\tau_{RC}}$) below ~ -80^{o} at 120 Hz. This highlights the critical requirement for EC) with low series resistance and high specific capacitance to ensure effective performance at frequencies in the hundreds of kilohertz range (1-4). Significant progress is being made in this crucial area (3-11).

In the literature, a phase angle of −80° is often used as a criterion for evaluating the frequency response of electrochemical capacitors (ECs). However, this does not imply that ECs lose their filtering functionality at higher frequencies when their phase angle exceeds −80°. In power distribution network (PDN) designs for electronics, a decoupling AEC remains effective until it reaches its self-resonant frequency, typically in the tens to hundreds of kilohertz range, where its phase angle reaches 0°. Developing compact ECs capable of operating in the hundreds of kilohertz range would significantly expand their applications, from 60 Hz line-frequency filtering to much broader markets.

In ECs, fast response is primarily limited by series resistance, which arises from the ionic resistance within the electrode pores and bulk electrolyte, as well as the electronic resistance of the electrodes. While electrolyte resistance is determined by the intrinsic mobility of ions, reducing the electrode's ionic resistance can be achieved by maintaining open porous structures that facilitate ion movement. However, straight-through open pores, though beneficial for ion mobility, reduce the available surface area for ion storage,

resulting in lower capacitance. Therefore, designing intricate porous structures is crucial to balance high specific capacitance with low series resistance (12-18).

In the early stages of developing ultrafast kHz ECs, it was recognized that the interface resistance between a carbon nanostructure and its metal current collector significantly limited the frequency response(1). To address this, several interfacial engineering solutions were implemented, particularly the direct deposition of vertically oriented graphene and CNTs (19-29). Subsequent efforts have primarily focused on achieving a large areal capacitance density by exploring various material-based electrode structures. Beyond carbon particles, CNTs, and graphene, other conductive materials such as MXenes, certain transition metal dichalcogenides, and transition metal oxides have also been investigated(9, 11, 30-37). In terms of device architecture, the lateral interdigital configuration was developed alongside the conventional electrode/separator/electrode sandwich architecture. However, the areal capacitance at 120 Hz (C_{A120}) generally remains below 1.5 mF cm^{-2} to meet the phase angle requirement.

To further enhance electrode capacitance density, the trend is to adopt a composite architecture with dense, macroscale pores for rapid double-layer formation by electrolytic ions at high transport rates. These pores are connected by a network that serves as a long-range pathway for ultrafast electron transport. This structure maximizes the contact area between the electrode and electrolyte, allowing efficient ion transport at high current rates. Only a few structures have recently demonstrated $C_{A120} > 2$ mF cm^{-2} (3, 4, 8, 9, 16, 38, 39), and some may face challenges in large-scale production due to the delicate processes involved—contrasting with the low cost of capacitors as electronic components.

We propose a method to create a freestanding nanostructured carbon electrode that enhances ion migration through a large porous area while maintaining low electrode resistance. The structure, derived by rapidly carbonizing a bacterial cellulose (BC) network embedded with zeolitic imidazolate framework 8 (ZIF-8) and in-situ formed carbon nanotubes (CNTs), is abbreviated as CNT-ZIF-8-CBC. In our previous work, caged structures like carbonized ZIF-67 and Prussian blue have shown excellent performance as electrodes of kHz high-frequency ECs (HF-ECs) due to their nanocage networks' ability to host ions (38, 40). The

synthesis of ZIF-8 can be controlled to a size of ~100 nm, allowing its uniform growth within the voids between individual BC nanofibers (41). In the resulting CNT-ZIF-8-CBC structure, carbonized BC (CBC) provides an interconnected three-dimensional carbon fibrous network, acting as an electronic highway(42). The carbonized ZIF-8 nanocages, formed by rapid vaporization of zinc centers and carbonization of organic linkers, create a porous structure with a large and easily accessible surface area(43-46). In-situ grown CNTs further link the dispersed nanocages to the CBC fibrous network. This process yields a freestanding electrode with an exceptionally low area resistance of 9.8 mΩ cm^2 and a specific capacitance of 2.1 mF cm^{-2} at 120 Hz, while maintaining excellent performance at kilohertz frequencies. Stacking these electrodes increases total capacitance to 5.3 mF cm^{-2}, though with slight phase response reduction. Additionally, we packaged three units in series in a coin-cell to extend the voltage window to 2.4 V, suitable for high-voltage applications. Analysis of filtering effects of these 2.4 V ECs under various loads and frequencies shows stable performance, effectively minimizing peak-to-peak ripple voltage from line frequency to 60 kHz, indicating strong ripple and noise filtering capabilities. These results underscore the potential of these nanostructured ECs as advanced filtering capacitors with a miniaturized design for next-generation electronic applications.

2.Results and Discussion

Material Synthesis and Characteristics

The fabrication of CNT-ZIF-8-CBC electrodes is illustrated schematically in Fig. 1a. Firstly, BC sheets (Fig. S1 in the supplementary information (SI)) were converted into BC fibers using a homogenizer. Nickel doped ZIF nanocages, approximately 100 nm in size, were synthesized inside the BC network using a solvothermal process. The dense hydroxyl functional groups on the BC nanofibers facilitated the nucleation, growth and dispersion of ZIF-8 nanocrystals along individual nanofibers (41). The obtained solution was vacuum filtrated to form free-standing membranes. After vacuum drying, the samples were heated directly at 950°C in nitrogen environment for only 20 minutes, resulting in rapid carbonization of ZIF-8-BC. Meanwhile, the introduced Ni impurities will induce new carbon nanotube growth. The newly grown carbon

nanotubes, in conjunction with carbonized BC nanofibers, connect the carbonized ZIF-8 cages to form a highly conductive, porous and freestanding CNT-ZIF-8-CBC carbon electrode.

Fig. 1b shows scanning electron microscope (SEM) image of CBC after carbonization at 950ºC, having a well-connected 3D network with high surface area and large pore volume to hold ZIF cages. The microscopic morphology of freestanding CNT-ZIF-8-CBC carbon electrode is presented in Fig. 1c, d and Fig. S2. The small pockets of carbonized ZIF act as storage sites and hence the uniform deposition of ZIF nanocages inside the BC network will improve the ion storage capacity of the material. A uniform ZIF deposition was observed, with subsequent CNT growth connecting these well dispersed nanocages and CBC nanofibers, as illustrated in SEM image in Fig. 1c and transmission electron microscopy (TEM) image in Fig. 1e. Notably, the ZIF-BC was subjected to instant evaporation of its organic groups and zinc centers in the rapid carbonization process, leading to the formation of porous nanocages. The rapid carbonization of ZIF distorts its caged structure with nanocage popup compared to a regular carbonization where the ZIF retains its caged structure with certain shrinkage (47, 48) as shown in Fig. S3. The high-angle annular dark field scanning-TEM (HAADF-STEM) image in Fig. 1f and S4 evidences the formation of carbon nanotubes facilitated by nickel nanoparticles in the sample. The HAADF-STEM image in Fig. 1g shows the nanocage popup behavior of the ~100 nm sized caged structures which leads to formation of pores on the ZIF facets. The nanocage popup facilitates electrolytic ions to rapidly access its surface area, greatly contributing to

the large capacitance at high frequencies. It is noted the electrode has a thickness of 15 µm (Fig. 1d).

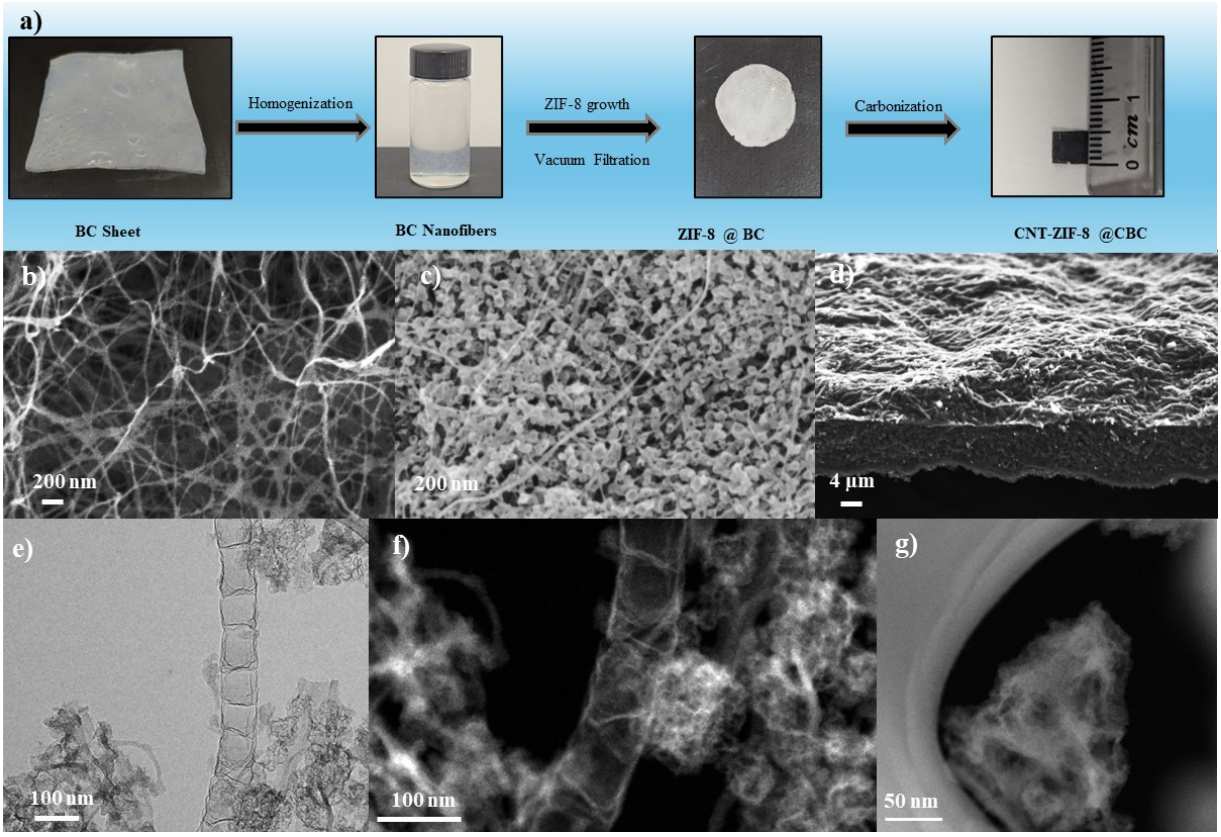

Figure 1. Schematic illustration of the CNT-ZIF-8-CBC electrode preparation process (a). SEM image of CBC (b) and CNT-ZIF-8-CBC (c and d). TEM image (e), HAADF-STEM image of CNT-ZIF-8-CBC (f). HAADF-STEM image of rapidly carbonized porous ZIF nanocages (g).

Porous features of the electrodes were characterized using Brunauer-Emmett-Teller (BET) measurements to determine their specific surface area and pore size distribution. Fig. S5a shows the N_2 adsorption-desorption curves for CNT-ZIF-8-CBC which features a hysteresis from medium to high P/P^o value suggesting the presence of mesopores and macropores. The initial steep slope also suggests the formation of micropores in the electrode. The presence of these porous ion storage sites can be seen in the pore size distribution curves in Fig. S5b. Hence, CNT-ZIF-8-CBC showed a surface area of 1338.5 m^2g^{-1} for the CNT-CBC-ZIF-8 electrodes compared to 273.0 m^2g^{-1} for CBC electrodes. ZIF-8 inclusion significantly increases the SSA of the electrodes.

The carbonized material was characterized using X-ray diffraction (XRD) analysis and Raman spectroscopy, as presented in Fig. S6a, b. The chemical elements and their bonds were studied using X-ray photoelectron spectroscopy (XPS). The survey scan of XPS (Fig. S6c) confirms the presence of both N and O in CNT-ZIF8-CBC, while concentration of N in CBC is trivial. A weak Ni signal was detected since small amounts of Ni remains after acid etching, encapsulated within the CNT structure (49). For CNT-ZIF8-CBC, high-resolution XPS C 1s spectrum (Fig. S6d) reveals the existence of C-C, C-N, C=N, and C=O bonds, consistent with literature (50), and N 1s spectrum (Fig. S6e) indicated a large amount of pyridinic N and graphitic N in addition to pyrrolic and oxidized N. These groups were absent in the CBC that only has C-C and C=O bonds (Fig. S6f). It is noted that nitrogen doping increases the electrical conductivity of carbon, and further improves its hydrophilicity, facilitating rapid electric double layer formation. Indeed, Fig. S7 shows that while CBC is not quite hydrophilic, water drops on CNT-ZIF8-CBC are immediately absorbed due to its extreme hydrophilic properties.

Aqueous HF-EC

We evaluated the electrochemical performance of these electrodes in 6 M aqueous KOH electrolyte by assembling coin cell-type devices with two symmetrical electrodes of CNT-ZIF-8-CBC. Their performance was characterized by using electrochemical impedance spectroscopy (EIS). The Nyquist plot in Fig. 2a shows an almost vertical line with a steep slope, suggesting CNT-ZIF-8-CBC with rapid ionic transport ability. These electrodes exhibit a low resistance of 39 mΩ, significantly lower than the 200 mΩ observed for CBC (Fig. S8a), implying that the growth of CNTs and carbonized ZIF-8 on CBC reduces electronic resistance and enhances ion transport in the electrode by forming wide porous structures. The corresponding area resistance of the electrode is only 9.8 mΩ cm^2.

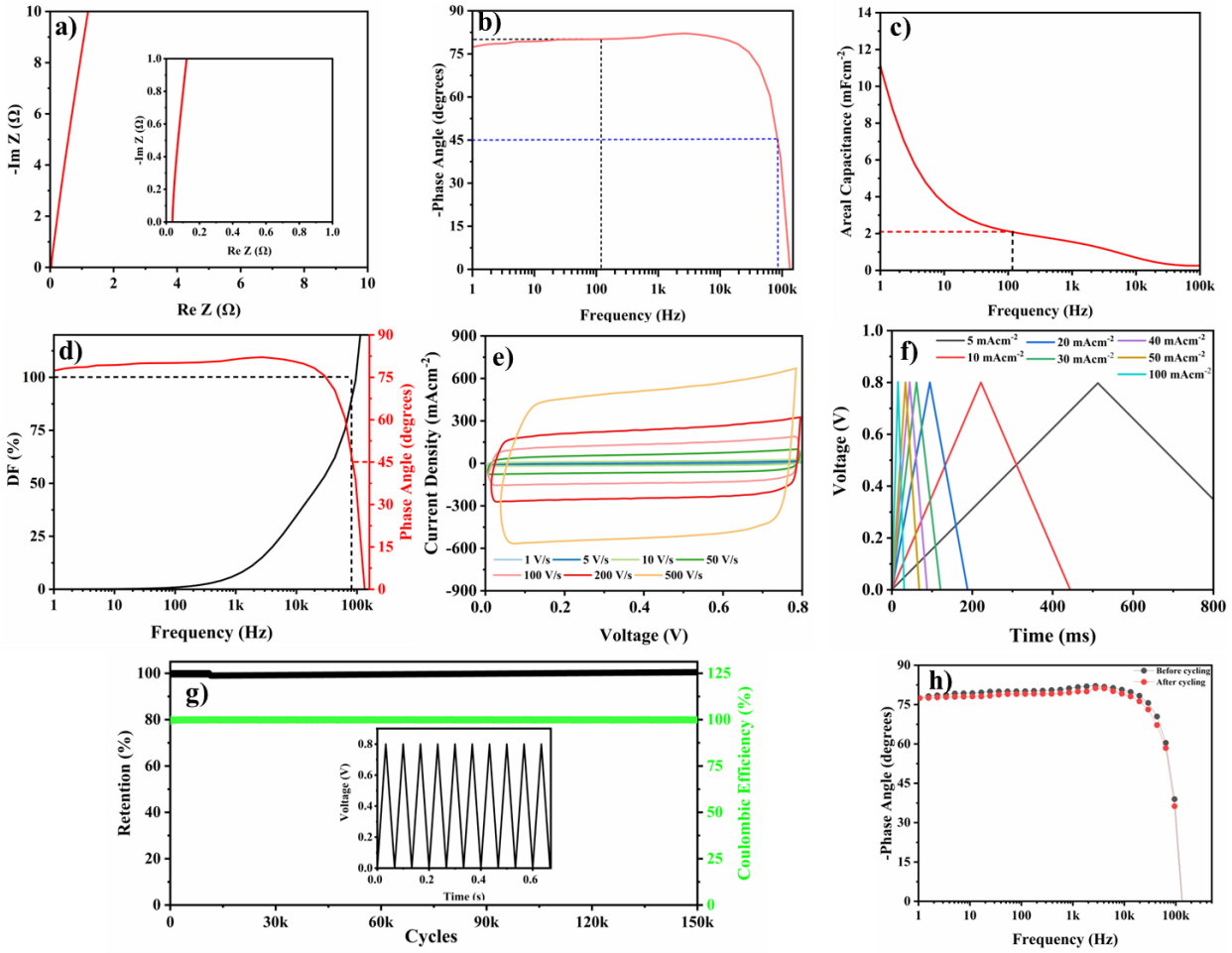

Figure 2. Nyquist Spectra (inset shows high frequency region) (a), Bode diagrams (b) and areal capacitance vs frequency plots (c) for CNT-ZIF-8-CBC in 6 M KOH electrolyte. Dissipation factor vs frequency (d), CV curves for different scan rates (e), GCD profiles for different current densities (f), long cycling performance at 50 $mAcm^{-2}$(g) and phase response after long cycling (h) for CNT-ZIF-8-CBC.

The Bode plot in Fig. 2b reveals that ECs based on CNT-ZIF-8-CBC have a phase response of - 80.3° at 120 Hz, and the phase angle even reaches - 82.1° at 2.5 kHz. Its frequency at – 45° phase angle is 79 kHz. In contrast, CBC-based ECs (Fig. S8b) have a smaller phase angle of -77° at 120 Hz and smaller frequency of 50 kHz at -45°. For CNT-ZIF-8-CBC electrodes, the presence of carbonized ZIF-8 particles on the CBC network partially impedes the formation of micropores in CBC, thereby improving the phase response at

lower frequencies(51). Additionally, the rapid carbonization of ZIF-8 cages creates more storage sites for ions, resulting in a high specific capacitance of 2.1 $mFcm^{-2}$ compared to 0.6 $mFcm^{-2}$ of CBC at 120 Hz (Fig. 2c and S8c). The former maintains an excellent capacitance of 1.56 $mFcm^{-2}$ even at 1 kHz, while the latter sustains a capacitance of 0.45 $mFcm^{-2}$. It is emphasized that at 120 Hz, even with a very large capacitance density of 2.1 $mFcm^{-2}$, the *RC* time constant, τ_{RC} for our HF-ECs is only 0.02 ms due to the exceptionally low ESR of 9.8 $m\Omega\ cm^2$, indicating its effectiveness as an efficient and compact line-frequency filtering capacitor.

The influence of electrode thickness on capacitive performance was investigated by synthesizing electrodes with thicknesses of 30 μm and 60 μm, as shown in Fig. S9. EIS comparisons among the three electrodes are presented in Fig. S10. An increase in thickness leads to a higher areal capacitance due to the availability of more storage sites along extended ionic pathways. However, the elongated pathways slow down ion transport, which increases resistance within the electrodes, as observed in the Nyquist plot and phase response in the Bode plot (Fig. S10a and b).

To further investigate the relationship between structure and capacitance, a CNT-ZIF-CBC electrode with 500 nm ZIF cage size was synthesized. The EIS data comparing electrodes with different ZIF cage sizes are presented in Fig. S11. The 500 nm ZIF cages provide larger pathways, enabling more efficient transport of K^+ and OH^- ions with solvated radii of 0.33 nm and 0.3 nm, respectively. This improved ion transport reduces the ESR and enhances the phase response. However, the larger cage size results in a reduced surface area, leading to a lower overall capacitance. These findings highlight the trade-off between ion transport efficiency and ion storage capacity in hierarchical porous structures, emphasizing the importance of balancing pore size distributions for optimized performance.

The dissipation factor (DF), defined as the ratio of the resistive (lossy) part of the impedance to the reactive (capacitive) part of the impedance ($DF = \omega RC$), is a measure of energy loss as heat in a capacitor when it is subjected to an ac field, which is relevant to the maximum power the capacitor can handle in ac filtering.

In high-power applications with large ripples, a low DF is ideal. As depicted in Fig. 2d, DF exhibits a value of approximately 25% at ~4.7 kHz, reaching 100% at the characteristic frequency of ~79 kHz, where the capacitive impedance equals the resistive impedance. Beyond this frequency, the resistive impedance surpasses the capacitive impedance. For low power microelectronics where ripple current is tiny and the capacitor has a low ESR, a large DF is tolerable. The device still behaves as a capacitor until its maximum frequency ~128 kHz where the phase angle reaches zero. This is the self-resonate frequency f_0 ($f_0 = \frac{1}{2\pi\sqrt{(ESL)C}}$) where ESL is its equivalent series inductance. At frequencies above this point, the device will behave as an inductor, with a positive phase angle. Our HF-EC functions as a filtering capacitor up to ~128 kHz.

The HF-ECs were further characterized using cyclic voltammetry (CV) and galvanostatic charge-discharge (GCD) techniques. With their ability of rapid ionic and electronic response, the CV curves of these devices (Fig. 2e) show nearly rectangular profile even for a scan rate of 500 Vs^{-1}. The specific capacitance (Fig. S12) derived from CV curves reach 2.35 mF cm^{-2} at 100 Vs^{-1}. Additionally, GCD tests were conducted at different current densities, as shown in Fig. 2f. The perfect triangular nature of the curves suggests almost no *IR* drop since the ESR is trivial. The electrode exhibits an areal capacitance of 1.9 mF cm^{-2} at a high current density of 100 mA cm^{-2}, maintaining 60% of the capacitance at 5 mA cm^{-2} (Fig. S13). To verify the durability, the HF-ECs were tested under continuous GCD at 50 $mAcm^{-2}$ for 150,000 cycles. The Coulombic efficiency was maintained at ~ 100% with almost no degradation of the capacitance (Fig. 2g). Similarly, an almost constant phase response was observed before and after the test (Fig. 2h).

A single layer of CNT-ZIF-8-CBC has a thickness of 15 μm. To increase the areal capacitance density, cells were assembled by stacking 2 or 3 layers as electrodes. EIS Bode plots and the frequency-dependent capacitance for these cells are shown in Figs. 3a, b. With increased ionic path through the stacked thick electrodes compared to a single-layer electrode, the phase response at 120 Hz decreases from -80.3º to

approximately ~76.8º and ~74.4º for these stacked electrodes. However, they retain a phase angle below −45° up to approximately 50 kHz, demonstrating excellent high-frequency performance. The obtained capacitive behavior indicates an increase in capacitance at 120 Hz to 3.8 mF cm^{-2} and 5.3 mF cm^{-2} for these cells. This demonstrates that stacking electrodes can improve the capacitance of the device at the cost of reduction in phase response.

We compared our capacitor with a commercial 6.3V AEC in terms of areal and volumetric capacitance. Fig. S14a and b clearly show the circuit miniaturization possibility using our HF-EC electrodes. Further, we compared our results with those reported in the literature based on areal capacitance and phase response at 120 Hz in Fig. 3c. Among them, graphene-based electrodes, high density carbon nanotube-based films and carbon structures derived from polymers like PEDOT and PSS, and MOFs show excellent capacitive behavior having phase angle above -80º while maintaining a capacitance above 0.5 mF cm^{-2} in most cases (9, 10, 14, 33, 52-58). Our HF-ECs using porous ZIF provide one of the best overall performances among these reported electrodes.

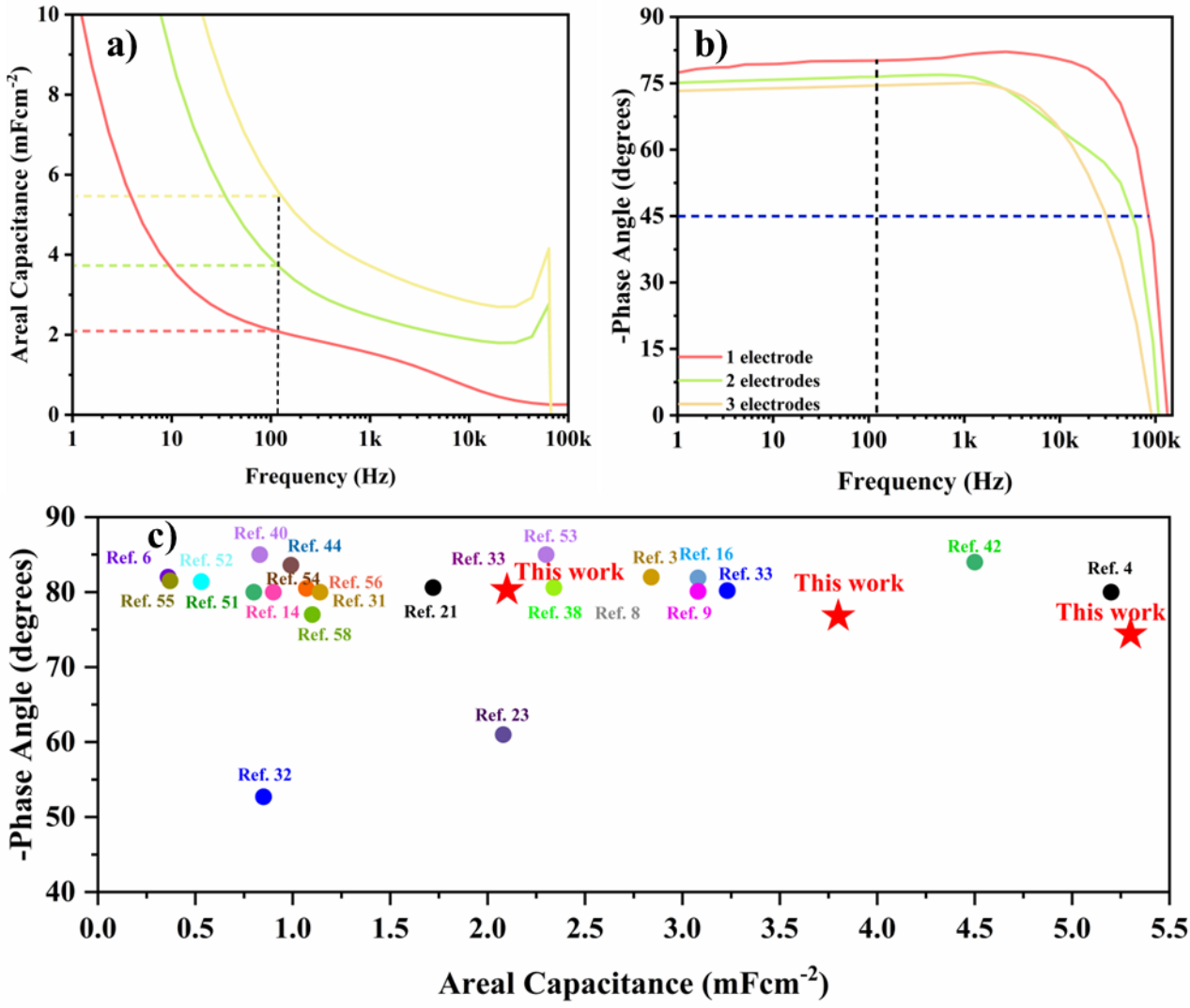

Figure 3. Bode diagrams (a), and areal capacitance vs frequency plots (b) for 1-3 layers of CNT-ZIF-8-CBC as electrodes. (c) Plot of results from this work in terms of areal capacitance and phase response at 120 Hz in comparison to other reported results using 6M KOH electrolyte or 1 M H_2SO_4.

Organic HF-EC

We explored the electrochemical behavior of electrodes in organic electrolytes to elucidate their performance at higher voltages. Specifically, we assembled devices with 1 M tetraethylammonium tetrafluoroborate ($TEABF_4$) in acetonitrile (ACN). Nyquist plots of EIS in Fig. 4a show a small semi-circle

indicative of increased solution resistance, attributed to the movement of larger ions in the organic electrolyte compared to aqueous electrolytes. This results in an increase in the ESR to 221 mΩ for CNT-ZIF-8-CBC. Further analysis in Fig. 4b and 4c shows a phase angle of approximately -78º at 120 Hz and a capacitance of 1.24 $mFcm^{-2}$. Additionally, the cyclic voltammetry (CV) curves in Fig. S16 exhibit a rectangular profile up to 200 Vs^{-1}.

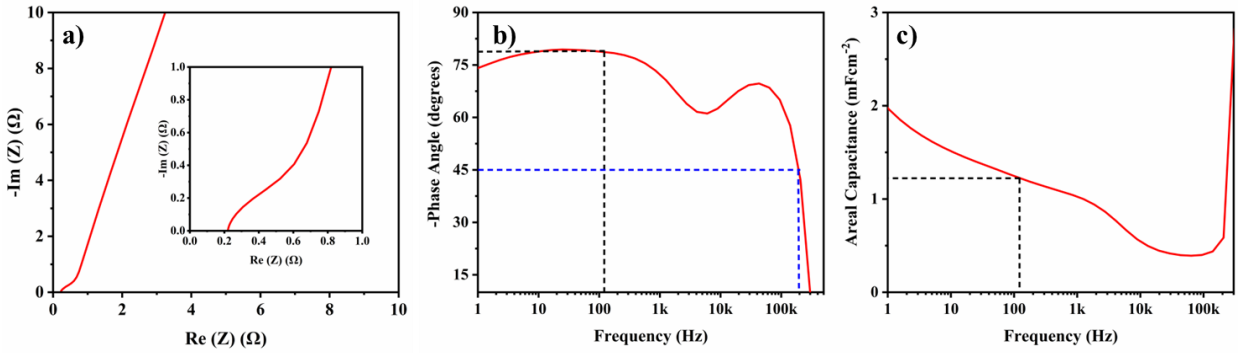

Figure 4. Nyquist Spectra (a), Bode diagram (b) and areal capacitance vs frequency plot (c), for CNT-ZIF-8-CBC electrode in organic electrolyte.

Cell Integration and Ripple Filtering Demonstration

The aqueous HF-EC limits the potential window of 0.8 V. To achieve a higher voltage window, three cells were assembled in series to reach a voltage of 2.4 V. Fig. 5a shows the CV curve of the integrated cell up to a stable voltage of 2.4 V. This integrated cell was tested as a filtering capacitor in an AC/DC converter, as shown in the schematic in Fig. 5b, which is composed of four rectifying diodes D1-D4, filtering capacitor C and load R. V_i is the input AC signal, V_o is the output voltage having a ripple voltage of V_r.

The ripple voltage is a critical parameter in filtering circuits that directly affects the stability and quality of the output power. In high-power applications, excessive V_r leads to increased power losses in the ESR of the filtering capacitor. These losses manifest as Joule heating, which can significantly reduce the efficiency of the power delivery system and limit the amount of ripple the capacitor can safely handle. If V_r exceeds a certain threshold, the excessive heat generated within the capacitor can cause thermal stress, potentially

damaging the component or shortening its lifespan. For voltage-sensitive systems, such as microchip power supplies, it is not only the power loss that is of concern but also the tolerable noise levels of the sensitive microchips. These systems often have stringent noise requirements, meaning the ripple voltage must be minimized to prevent interference with the performance of the microchips. In these cases, the maximum V_r is determined by the microchip's tolerance for noise and signal integrity, which typically requires very low ripple voltages to ensure stable operation and prevent data corruption or malfunctions (59, 60).

For a sine wave at frequency *f* as the input, the ripple voltage from the AC/DC converter is given by $V_r \approx \frac{V_o - 2V_d}{2fCR}$, where V_o is the output voltage having a ripple voltage of V_r, V_d is the voltage drop on each diode, and C and R are the filtering capacitor and load, respectively. Therefore, with a given load, a large capacitance favors a lower ripple voltage. We tested the integrated HF-EC at a constant 60 Hz frequency with different waveforms and varied loads, as shown in Fig. 5c-f. The ripple voltage (V_r) observed for a 470 Ω load with a square waveform is approximately ~0.06 V, while for a sine waveform, it is ~0.1 V. The ripple voltage decreases further to ~0.04 V during the 100 kΩ load test, with a similar trend observed for other waveforms.

An alternative method to achieve a higher operating window is to assemble the electrodes with an organic electrolyte, as demonstrated with a working potential up to 2.5 V. The cell was tested at 60 Hz with four different waveforms and load variations. The observed ripple voltage was approximately ~0.04 V at a 2.2 kΩ load (Fig. S17 in SI). Testing the same cell at a constant load of 470 Ω and increasing the frequency up to 60 kHz (Fig. S18 in SI) showed a consistent trend in ripple voltage, indicating a nearly pure DC signal at higher frequencies. Some noise was observed, which is associated with measurement artifacts and not ripple voltage, as it lacks a distinct pattern.

For practical applications, three aqueous cells were assembled in series to form an integrated device as shown in figure S19a. It was used to test the ripple in an LED. The input AC signal to the LED was generated by a waveform generator having a frequency of 20 Hz as seen in Fig. S19. The flickering response

of the LED was recorded as seen in video V1 in SI. A bench vise is used to hold the capacitor firmly between two copper plates. The constant flickering of the LED changed into a stable light when the capacitor is plugged in the circuit due to smooth filtered DC signal as seen in video V2 in SI. The filtered signal using the device is shown in Fig. S19b. These proof-of-concept tests suggest that the CNT-ZIF-8-CBC electrode shows promise as an excellent material for high-frequency EC applications.

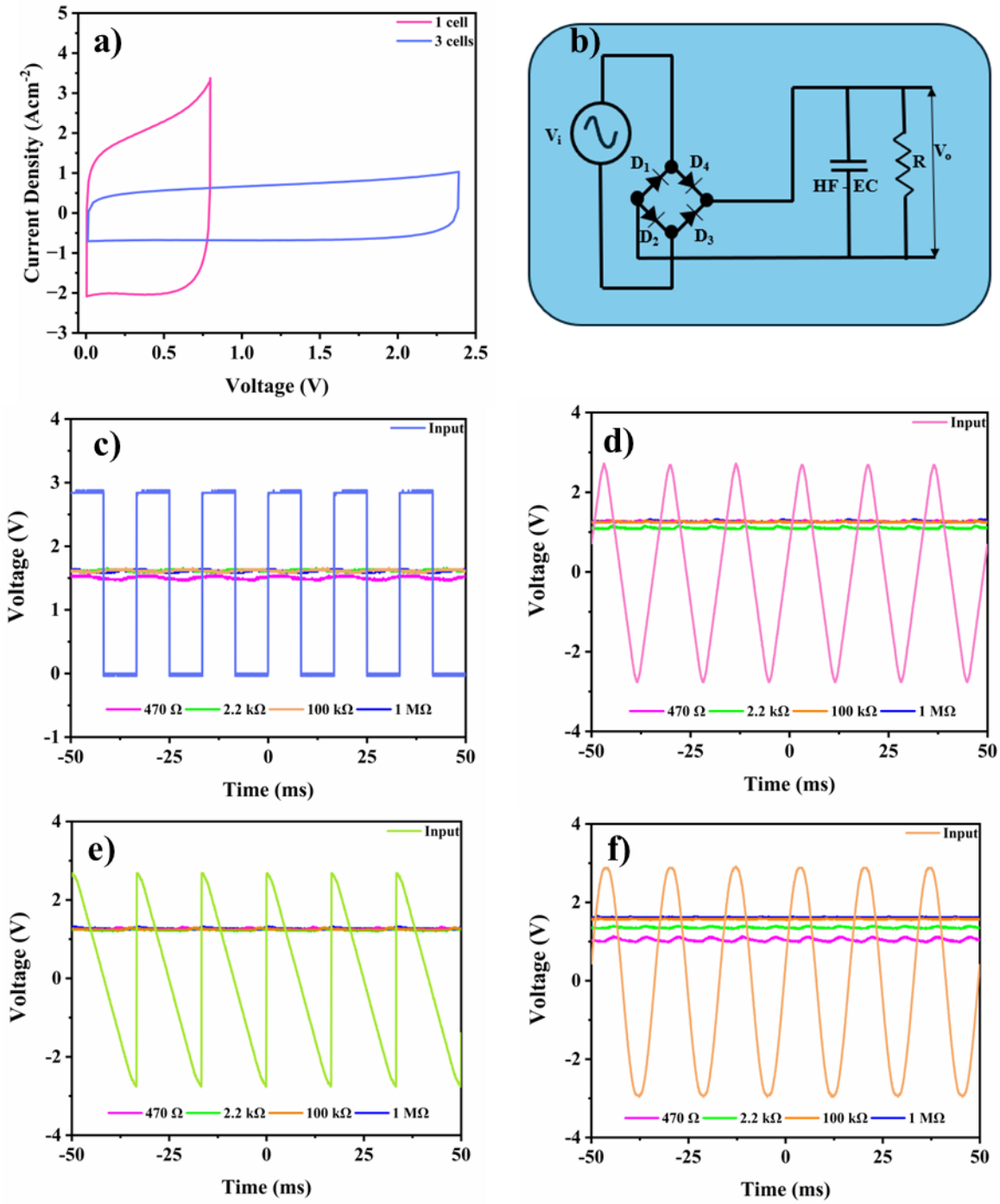

Figure 5. (a) CV curve of 1 and 3 cell in series connection. (b) Schematic circuit for AC/DC full wave conversion using HF-EC capacitor. Measured load voltage with series integrated HF-EC filtering at different loads and *f*= 60 Hz for (c) sinusoidal, (d) ramped, (e) square and (f) triangular input waveform.

3. Conclusion:

We developed a freestanding nanostructured carbon electrode, CNT-ZIF-8-CBC, by rapidly carbonizing a bacterial cellulose network embedded with ZIF-8 and in-situ growth of carbon nanotubes. This electrode features a large porous surface area for enhanced ion migration and low resistance, achieved through interconnected CNT, carbon nanofibers and nanocages. The resulting 15 μm thick structure offers low area resistance (9.8 mΩ cm^2) and high specific capacitance (2.1 mF cm^{-2} at 120 Hz), maintaining strong performance at kilohertz frequencies. Stacking these electrodes boosts capacitance to 5.3 mF cm^{-2}, with a slight phase response reduction. When packaged in series to extend the voltage window to 2.4 V, the system shows stable ripple and noise filtering performance across a wide frequency range, demonstrating its potential for next-generation filtering capacitors.

4. Materials and Methods:

4.1. Material Synthesis:

Bacterial Cellulose sheets (6 x 4 x 0.5 cm) were impelled in methanol solution. The solution was diluted and ultrasonicated to form a uniform dispersion. The obtained solution was centrifuged to remove chunky agglomerated BC fibers. 1.07 g of $Zn(NO_3)_2.6H_2O$ and 0.0924 g of $Ni(acac)_2$ was added to 50 mL of this dispersed BC solution and stirred for 12 hours. Another solution of organic linkers was made by adding 2.36 g of 2-methylimidazole in 50 mL of methanol. Both the solutions were mixed and sonicated for one hour. The mixed solution was transferred into a 100 mL stainless-steel autoclave and underwent solvothermal reaction for 4 hours at 120°C. 5 mL of the solution was taken and diluted with methanol and ultrasonicated for 1 hour. A free-standing membrane was formed from this solution using vacuum filtration. The membranes were washed with methanol to remove any unreacted linkers followed by drying in vacuum at 100°C overnight. The membranes were then transferred inside a tube furnace where the free-standing membranes were kept inside a covered boat with ground dicyandiamide (DCD). Typically, a 4:1 ratio by mass of the film to DCD was used. The tube furnace was ramped at 5°C/min to 950°C and the samples

were inserted into the heating zone of the tube furnace for 20 minutes in a nitrogen environment. These samples were labelled as CNT-ZIF-8-CBC. These samples were cleaned with 6M HCl for 12 hours to remove the nickel nanoparticles. These films were washed with DI water and then dried. The samples were finally heated in nitrogen environment at 300ºC for 1 hour to remove chlorine ions from the samples. The samples directly carbonized from BC were labelled as CBC. The carbonized films were cut into 5 mm x 5mm sheets with a thickness of 15µm.

4.2. Material Characterization:

The morphology of the sample was characterized using Scanning Electron Microscopy (SEM) on Zeiss Auriga. X-Ray Diffraction (XRD) patterns were recorded with Malvern PANalytical Aeris. The X-ray photoelectron spectroscopy (XPS) was conducted with the help of Kratos Axis Supra. Raman spectra was collected using a custom-built Raman spectrometer with a 180° geometry. High–angle annular dark–field scanning transmission electron microscopy (HAADF–STEM) and elemental mapping were recorded on Themis microscopy at the University of Connecticut. Dcorr+ spherical probe corrector is equipped with this microscope giving best spatial resolution of 0.08 nm. SuperX G1 was used for a highly efficient STEM-EDX elemental mapping with 0.7 sr EDX collection angle.

4.3. Electrochemical Measurements:

Symmetric cells were assembled with these electrodes and 6 M KOH as aqueous electrolyte and a hydrophilic separator in a 2032-coin cell. The area of each electrode was 0.25 cm^2. All measurements were carried out in Biologic SP-150 electrochemical workstation. Cyclic Voltammetry (CV) was performed in a voltage window of 0-0.8V using scan rates from 1 mVs^{-1} to 500 Vs^{-1} for aqueous HF-ECs and 0-2.5 V using scan rates from 1-200 Vs^{-1} for organic HF-ECs. EIS was performed in the frequency range of 1 MHz to 0.1 Hz with 10 mV AC signal. Galvanostatic charge-discharge (GCD) measurements were conducted in a current density range varying from 5 to 100 $mAcm^{-2}$ in a voltage range of 0-0.8V for aqueous electrolytes. For high voltage aqueous cells, three sub-cells are stacked in series and packed into one 2032 coin-cell.

Acknowledgements

This work was supported by the National Science Foundation under Grant 2122921. The TEM studies were performed using the facilities in UConn/Thermo Fisher Scientific Center for Advanced Microscopy and Materials Analysis.

References:

1. Miller JR, Outlaw R, Holloway B. Graphene double-layer capacitor with ac line-filtering performance. **Science**. 2010;329(5999):1637-9.
2. Fan Z, Islam N, Bayne SB. Towards kilohertz electrochemical capacitors for filtering and pulse energy harvesting. **Nano Energy**. 2017;39:306-20.
3. Han F, Qian O, Meng G, Lin D, Chen G, Zhang S, Pan Q, Zhang X, Zhu X, Wei B. Structurally integrated 3D carbon tube grid–based high-performance filter capacitor. **Science**. 2022;377(6609):1004-7.
4. Hu Y, Wu M, Chi F, Lai G, Li P, He W, Lu B, Weng C, Lin J, Chen F. Ultralow-resistance electrochemical capacitor for integrable line filtering. **Nature**. 2023;624(7990):74-9.
5. El-Kady MF, Strong V, Dubin S, Kaner RB. Laser scribing of high-performance and flexible graphene-based electrochemical capacitors. **Science**. 2012;335(6074):1326-30.
6. Ren G, Pan X, Bayne S, Fan Z. Kilohertz ultrafast electrochemical supercapacitors based on perpendicularly-oriented graphene grown inside of nickel foam. **Carbon**. 2014;71:94-101.
7. Kyerematen NA, Brousse T, Pech D. Microsupercapacitors as miniaturized energy-storage components for on-chip electronics. **Nature nanotechnology**. 2017;12(1):7-15.
8. Zhang M, Dong K, Saeedi Garakani S, Khorsand Kheirabad A, Manke I, Wu M, Wang H, Qu L, Yuan J. Bridged Carbon Fabric Membrane with Boosted Performance in AC Line-Filtering Capacitors. **Advanced Science**. 2022;9(7):2105072.
9. Chen G, Han F, Lin D, Zhang S, Pan Q, Shao C, Wang Z, Zhu X, Meng G, Wei B. Three-dimensional multi-layer carbon tube electrodes for AC line-filtering capacitors. **Joule**. 2024;8(4):1080-91.
10. Chi F, Li C, Zhou Q, Zhang M, Chen J, Yu X, Shi G. Graphene-based organic electrochemical capacitors for AC line filtering. **Advanced Energy Materials**. 2017;7(19):1700591.
11. Ma X, Sha J, Chen B, Shi C, Ma L, Wang H, Zhao N, Kang J. Recent progress on Materials and Structure of Supercapacitors for AC Line Filtering Application. **Journal of Materials Chemistry A**. 2024.
12. Zhang M, Wang W, Tan L, Eriksson M, Wu M, Ma H, Wang H, Qu L, Yuan J. From wood to thin porous carbon membrane: Ancient materials for modern ultrafast electrochemical capacitors in alternating current line filtering. **Energy Storage Materials**. 2021;35:327-33.

13. Gund GS, Park JH, Harpalsinh R, Kota M, Shin JH, Kim T-i, Gogotsi Y, Park HS. MXene/polymer hybrid materials for flexible AC-filtering electrochemical capacitors. **Joule**. 2019;3(1):164-76.
14. Suh S, Kim K, Park J, Kim W. Ultrafast flexible PEDOT: PSS supercapacitor with outstanding volumetric capacitance for AC line filtering. **Chemical Engineering Journal**. 2023;463:142377.
15. Tang H, Tian Y, Wu Z, Zeng Y, Wang Y, Hou Y, Ye Z, Lu J. AC line filter electrochemical capacitors: materials, morphology, and configuration. **Energy Environmental Materials**. 2022;5(4):1060-83.
16. Zhao M, Qin Y, Wang X, Wang L, Jin Q, Song M, Wang X, Qu L. PEDOT: PSS/Ketjenblack Holey Nanosheets with Ultrahigh Areal Capacitance for kHz AC Line-Filtering Micro-Supercapacitors. **Advanced Functional Materials**. 2024;34(12):2313495.
17. Li Z, Wang X, Zhao L, Chi F, Gao C, Wang Y, Yan M, Zhou Q, Zhao M, Wang X. Aqueous hybrid electrochemical capacitors with ultra-high energy density approaching for thousand-volts alternating current line filtering. **Nature Communications**. 2022;13(1):6359.
18. Xue J, Gao Z, Xiao L, Zuo T, Gao J, Li D, Qu L. An ultrafast supercapacitor based on 3D ordered porous graphene film with AC line filtering performance. **Applied Energy Materials**. 2020;3(6):5182-9.
19. Cai M, Outlaw RA, Quinlan RA, Premathilake D, Butler SM, Miller JR. Fast response, vertically oriented graphene nanosheet electric double layer capacitors synthesized from C2H2. **Acs Nano**. 2014;8(6):5873-82.
20. Miller JR, Outlaw RA. Vertically-oriented graphene electric double layer capacitor designs. **Journal of The Electrochemical Society**. 2015;162(5):A5077.
21. Xu S, Wen Y, Chen Z, Ji N, Zou Z, Wu M, Qu L, Zhang J. Vertical graphene arrays as electrodes for ultra-high energy density AC line-filtering capacitors. **Angewandte Chemie**. 2021;133(46):24710-4.
22. Sahoo S, Sahoo G, Jeong SM, Rout CS. A review on supercapacitors based on plasma enhanced chemical vapor deposited vertical graphene arrays. **Journal of Energy Storage**. 2022;53:105212.
23. Rangom Y, Tang X, Nazar LF. Carbon nanotube-based supercapacitors with excellent ac line filtering and rate capability via improved interfacial impedance. **ACS nano**. 2015;9(7):7248-55.
24. Yoo Y, Kim S, Kim B, Kim W. 2.5 V compact supercapacitors based on ultrathin carbon nanotube films for AC line filtering. **Journal of Materials Chemistry A**. 2015;3(22):11801-6.
25. Qi JL, Wang X, Lin JH, Zhang F, Feng JC, Fei W-D. A high-performance supercapacitor of vertically-oriented few-layered graphene with high-density defects. **Nanoscale**. 2015;7(8):3675-82.
26. Bundaleska N, Felizardo E, Santhosh N, Upadhyay K, Bundaleski N, Teodoro O, do Rego AB, Ferraria A, Zavašnik J, Cvelbar U. Plasma-enabled growth of vertically oriented carbon nanostructures for AC line filtering capacitors. **Applied Surface Science**. 2024;676:161002.
27. Yoo Y, Kim M-S, Kim J-K, Kim YS, Kim W. Fast-response supercapacitors with graphitic ordered mesoporous carbons and carbon nanotubes for AC line filtering. **Journal of Materials Chemistry A**. 2016;4(14):5062-8.
28. Xu S, Shen C, Peng Z, Wu J, Chen Z, Zhang X, Ji N, Jian M, Wu M, Gao X. Direct Growth of Vertical Graphene on Fiber Electrodes and Its Application in Alternating Current Line-Filtering Capacitors. **ACS nano**. 2024.
29. Jiang Q, Kurra N, Maleski K, Lei Y, Liang H, Zhang Y, Gogotsi Y, Alshareef HN. On-chip MXene microsupercapacitors for AC-line filtering applications. **Advanced Energy Materials**. 2019;9(26):1901061.
30. Feng X, Wang S, Das P, Shi X, Zheng S, Zhou F, Ning J, Wang D, Zhang J, Hao Y. Ultrahigh-rate and high-frequency MXene micro-supercapacitors for kHz AC line-filtering. **Journal of Energy Chemistry**. 2022;69:1-8.

31. Wen Y, Chen H, Wu M, Li C. Vertically oriented MXene bridging the frequency response and capacity density gap for ac-filtering pseudocapacitors. **Advanced Functional Materials**. 2022;32(21):2111613.
32. Tang H, Xia K, Lu J, Fu J, Zhu Z, Tian Y, Wang Y, Liu M, Chen J, Xu Z. NiTe2-based electrochemical capacitors with high-capacitance AC line filtering for regulating TENGs to steadily drive LEDs. **Nano Energy**. 2021;84:105931.
33. Chen G, Han F, Ma H, Li P, Zhou Z, Wang P, Li X, Meng G, Wei B. High Density 3D Carbon Tube Nanoarray Electrode Boosting the Capacitance of Filter Capacitor. **Nano-Micro Letters**. 2024;16(1):235.
34. Yoo Y, Park J, Kim M-S, Kim W. Development of 2.8 V Ketjen black supercapacitors with high rate capabilities for AC line filtering. **Journal of Power Sources**. 2017;360:383-90.
35. Mariappan VK, Krishnamoorthy K, Manoharan S, Pazhamalai P, Kim SJ. Electrospun polymer-derived carbyne supercapacitor for alternating current line filtering. **Small**. 2021;17(34):2102971.
36. Chen Z, Chen Y, Zhao Y, Qiu F, Jiang K, Huang S, Ke C, Zhu J, Tranca D, Zhuang X. B/N-enriched semi-conductive polymer film for micro-supercapacitors with AC line-filtering performance. **Langmuir**. 2021;37(7):2523-31.
37. Kang JG, Kim M, Kim PD, Ju BK, Kim SK. Three-dimensional mesostructured single crystalline Fe3O4 for ultrafast electrochemical capacitor electrode with AC line filtering performance. **International Journal of Energy Research**. 2022;46(3):3490-501.
38. Li W, Azam S, Dai G, Fan Z. Prussian blue based vertical graphene 3D structures for high frequency electrochemical capacitors. **Energy Storage Materials**. 2020;32:30-6.
39. Jin Q, Khandelwal M, Kim W. Ultrafast high-capacitance supercapacitors employing carbons derived from Al-based metal-organic frameworks. **Energy Storage Materials**. 2024;70:103464.
40. Li W, Islam N, Azam S, Xu Z, Warzywoda J, Fan Z. ZIF-67-derived edge-oriented graphene clusters coupled with carbon nanotubes containing encapsulated Co nanoparticles for high-frequency electrochemical capacitors. **Sustainable Energy Fuels**. 2019;3(11):3029-37.
41. Lin X, Li W, Nguyen V, Wang S, Yang S, Ma L, Du Y, Wang B, Fan Z. Fe-single-atom catalyst nanocages linked by bacterial cellulose-derived carbon nanofiber aerogel for Li-S batteries. **Chemical Engineering Journal**. 2023;477:146977.
42. Islam N, Li S, Ren G, Zu Y, Warzywoda J, Wang S, Fan Z. High-frequency electrochemical capacitors based on plasma pyrolyzed bacterial cellulose aerogel for current ripple filtering and pulse energy storage. **Nano Energy**. 2017;40:107-14.
43. Zhang P, Sun F, Shen Z, Cao D. ZIF-derived porous carbon: a promising supercapacitor electrode material. **Journal of Materials Chemistry A**. 2014;2(32):12873-80.
44. Li X, Wu C, Zhu Z, Lu Z, Zhao Y, Zhang X, Zhou J-Y, Zhang Z, Pan X, Xie E. Decoration of ultrathin porous zeolitic imidazolate frameworks on zinc–cobalt layered double hydroxide nanosheet arrays for ultrahigh-performance supercapacitors. **Journal of Power Sources**. 2020;450:227689.
45. Xue J, Zhao Y, Yu L, Guo S. Preparation of nitrogen-doped carbon pyrolyzed from ZIF-8 and its performance in electrocatalytic oxygen reduction to hydrogen peroxide. **Journal of Electroanalytical Chemistry**. 2024;960:118202.
46. Yang Q, Liu R, Pan Y, Cao Z, Liu Y, Wang L, Yu J, Song H, Ye Z, Zhang S. ZIF-8-derived N-doped porous carbon wrapped in porous carbon films as an air cathode for flexible solid-state Zn-air batteries. **Journal of Colloid and Interface Science**. 2022;628:691-700.
47. Cui J, Wang L, Han Y, Liu W, Li Z, Guo Z, Hu Y, Chang Z, Yuan Q, Wang J. ZnO nano-cages derived from ZIF-8 with enhanced anti mycobacterium-tuberculosis activities. **Journal of Alloys Compounds**. 2018;766:619-25.

48. Xue C, Zhao W, Zhang Q, Wang J, Wei Y, Lv K, Wu T, Lin Y, Li X, Hao X. From salt-filled ZIF-8 to open-door nanoporous carbon with optimized pore system for electrochemical supercapacitor with enhanced energy density. **Journal of Energy Storage**. 2022;51:104421.
49. Wang T, Yang J, Chen J, He Q, Li Z, Lei L, Lu J, Leung MK, Yang B, Hou Y. Nitrogen-doped carbon nanotube-encapsulated nickel nanoparticles assembled on graphene for efficient CO2 electroreduction. **ACS applied energy materials**. 2020;31(6):1438-42.
50. Yang H, Lin Q, Zhang C, Yu X, Cheng Z, Li G, Hu Q, Ren X, Zhang Q, Liu J. Carbon dioxide electroreduction on single-atom nickel decorated carbon membranes with industry compatible current densities. **Nature communications**. 2020;11(1):593.
51. Bal S, Baranwal R, Lin X, Li W, Yang S, Islam N, Fan Z. MoS2 nanoflakes based kilohertz electrochemical capacitors. **Batteries Supercaps**. 2024;7(1):e202300363.
52. Zhang M, Yu X, Ma H, Du W, Qu L, Li C, Shi G. Robust graphene composite films for multifunctional electrochemical capacitors with an ultrawide range of areal mass loading toward high-rate frequency response and ultrahigh specific capacitance. **Energy Environmental Science**. 2018;11(3):559-65.
53. Premathilake D, Outlaw RA, Quinlan RA, Parler SG, Butler SM, Miller JR. Fast response, carbon-black-coated, vertically-oriented graphene electric double layer capacitors. **Journal of The Electrochemical Society**. 2018;165(5):A924.
54. Zhang M, Zhou Q, Chen J, Yu X, Huang L, Li Y, Li C, Shi G. An ultrahigh-rate electrochemical capacitor based on solution-processed highly conductive PEDOT: PSS films for AC line-filtering. **Energy Environmental Science**. 2016;9(6):2005-10.
55. Islam N, Warzywoda J, Fan Z. Edge-oriented graphene on carbon nanofiber for high-frequency supercapacitors. **Nano-Micro Letters**. 2018;10:1-8.
56. Islam N, Hoque MNF, Li W, Wang S, Warzywoda J, Fan Z. Vertically edge-oriented graphene on plasma pyrolyzed cellulose fibers and demonstration of kilohertz high-frequency filtering electrical double layer capacitors. **Carbon**. 2019;141:523-30.
57. Li Z, Zhao L, Zheng X, Lin P, Li X, Li R, Han D, Zhao S, Lv D, Wang L. Continuous PEDOT: PSS nanomesh film: Towards aqueous AC line filtering capacitor with ultrahigh energy density. **Chemical Engineering Journal**. 2022;430:133012.
58. Ji N, Park J, Kim W. CMK-5-based high energy density electrical double layer capacitor for AC line filtering. **ACS omega**. 2019;4(20):18900-7.
59. Feng X, Shi X, Ning J, Wang D, Zhang J, Hao Y, Wu Z-S. Recent advances in micro-supercapacitors for AC line-filtering performance: From fundamental models to emerging applications. **EScience**. 2021;1(2):124-40.
60. Eftekhari A. The mechanism of ultrafast supercapacitors. **Journal of Materials Chemistry A**. 2018;6(7):2866-76.